Dalton Transactions

ROYAL SOCIETY OF CHEMISTRY

PAPER

View Article Online
View Journal | View Issue

Cite this: *Dalton Trans.*, 2025, **54**, 4096

Metal–ligand and hydrogen bonding in the active site of Fe(III)-, Mn(III)- and Co(III)-myoglobins†

Marek Freindorf and Elfi Kraka *

We investigated in this work the strength of metal–ligand bonding in complexes formed between Fe(III)-, Mn(III)- and Co(III)-myoglobin and methanol, water, nitrite, and azide, serving as neutral and ionic prototype ligands, for the ε and δ protonation forms of the myoglobin distal histidine. In total, 24 complexes and 12 associated gas phase models were investigated combining a QM/MM protocol with our local vibrational mode analysis at the PBE0/6-31G(d,p)/AMBER level of theory. According to our results, complexes with methanol and water ligands form weaker metal–ligand bonds than those with nitrite and azide ligands. Furthermore, the strength of the metal–ligand bonds depends on the protonation form of the distal histidine. Among the three metals investigated in this study, Fe, the metal found in native myoglobin, turned out to be the most versatile candidate, providing the broadest range of metal–ligand bond strengths. We also analyzed potential hydrogen bonds formed between the ligand and the distal histidine of the heme pocket. The ε tautomer of histidine forms weaker O···H type hydrogen bonds whereas the δ tautomer forms stronger N···H type hydrogen bonds. Overall, our findings identify the strength of both metal–ligand and hydrogen bonds (fully captured by our local vibrational mode analysis) as a key parameter determining the catalytic activity and function of myoglobins. This is particularly relevant when considering neutral *versus* ionic ligands and other metals such as Mn or Co as alternatives to Fe. The insights gained through our investigation offer valuable guidance for strategically fine-tuning existing artificial myoglobins and designing new, versatile variants. We hope that our QM/MM – local mode analysis protocol will become a valuable addition to the research community's toolkit.

Received 20th November 2024,
Accepted 7th January 2025

DOI: 10.1039/d4dt03246b

rsc.li/dalton

1 Introduction

Myoglobin (Mb) is a member of the hemoprotein superfamily, which is found in muscles of vertebrates and in almost all mammals. Mb is responsible for storage of oxygen in vertebrates and plays an important role in many physiological functions of the heart and skeletal muscles. It is also one of the most studied proteins disclosing interactions between the protein active site and the surrounding protein environment.[1–4] The active site of Mb includes a prosthetic heme group, which involves a protoporphyrin ring and a central Fe atom. The heme group is attached to the protein backbone by a covalent chemical bond with the proximal histidine, while the distal heme pocket can be occupied by small molecules such as O_2, NO, H_2S and CO, which are responsible for Mb's diverse biochemical activities.

Over the past decade a number of artificial Mb, *i.e.*, functionalized, bioengineered, or synthetic Mb proteins have been reported being intended to adapt Mother Nature's unique design to the specific needs across chemistry and beyond with applications in catalysis potentially replacing less sustainable and environmental friendly industrial catalysts; such as in medicine helping maintain oxygen delivery in situations where blood transfusions are limited or unavailable,[5] or as biosensors detecting oxygen or other gases.[6,7] In addition, they are ideal research models in experiment and theory, providing a controlled model to study heme protein function, protein folding, and oxygen storage mechanisms.

There are a number of reports applying artificial Mbs to various challenging catalytic transformations, bridging the gap between the efficiency of enzymatic reactions and the versatility of transition metal catalysis. Iron porphycene complexes of Mb used for selective CH functionalization reactions offer innovative ways to form CC, CN and CO bonds, such as cyclopropanation, amination, and azide reduction.[8–13] The iron porphyrin cofactor makes heme proteins particularly well-suited as catalysts for nitrene transfer reactions, including the reduction of azides to amines.[10] An engineered Mb-based catalyst has shown to be capable of catalyzing the cyclopropana-

Chemistry Department, Southern Methodist University, 3215 Daniel Avenue, Dallas, TX 75275, USA. E-mail: ekraka@smu.edu

†Electronic supplementary information (ESI) available: Plots of additional properties of HBs in the investigated protein systems, pictures of active sites in the proteins and the gas phase, and optimized coordinates of the active sites. See DOI: https://doi.org/10.1039/d4dt03246b

tion of aryl-substituted olefins with catalytic proficiency and excellent diastereo- and enantioselectivity *via* transmetalation.[14]

Replacement of Fe in hemoproteins by different transition metals has been utilized to investigate the role of heme in determining the protein properties for many years,[15–17] and the most popular metals used in the modified hemoproteins are Mn and Co.[18,19] Some recent examples of the Mn-substituted Mb (MnMb) include the discovery of two redox pathways in MnMb,[20] CH bond hydroxylation catalyzed in MnMb,[21,22] and oxidation properties of MnMb towards weak CH bonds.[23] Similarly, examples of Mn-substituted cytochromes P450 include structural properties of Mn-substituted P450 (CYP101),[24] theoretical study of the pentacoordinate Mn in cytochrome $P450_{cam}$,[25] catalytic activity of Mn-substituted cytochrome P450(BSb),[26] reconstruction of Mn-substituted cytochrome P450(BM3).[27–29] The Mn metal was also used in Mn-substitution of an abiological protein in a study of a porphyrin-binding protein with high-valent Mn oxidation states.[30]

Similarly, recent examples of Co-substituted Mb (CoMb) involve theoretical study of dioxygen bound to CoMb,[31] relaxation of ligand binding in CoMb,[32] nitrogen generation in CoMb,[33] and reconstruction of aqua- and cyano-CoMb.[34] Cobalt was also used in metal-substituted cystathionine β-synthase,[35] hydrogen generation from Co-substituted microperoxidase-11[36] and cytochrome b_{562},[37] reconstruction of CoMb-coupled histidine kinase,[38] and Co-substitution in a series of hemoproteins in living cells of *E. coli*.[39] CoMb complexes were used to catalyze electro-catalytic H_2 evaluation.[40,41] Heme oxygenase cobalt–protoporphyrin complexes were used for CO_2 photoreduction.[42] The Figg group has also introduced zinc–Mbs as catalyst for photo-induced electron/energy transfer (PET)-reversible addition–fragmentation chain transfer (RAFT) polymerizations.[43]

In order to systematically explore the large potential of these Fe, Co, Mn–Mbs, fine-tuning them for a specific purpose and/or the development of new design routes for artificial Mbs, the understanding of metal–ligand (ML) and potential ligand hydrogen bonding (HB) in the active Mb pocket at the molecular level is an important prerequisite, which to our best knowledge has been missing so far.

Therefore, inspired by the structural study of Mn- and Co-substituted Mb,[18] we explored in this study similarities or differences between native Fe(III)Mb, and the engineered Mn (III)Mb and Co(III)Mb systems with methanol (CH_3OH, MET), water (H_2O, H_2O), nitrite (NO_2^-, ONO), and azide (N_3^-, NNN) model ligands in the heme distal pocket, with a focus on assessing and comparing the strength of the ML bonds and the strength of potential HB interactions, formed between the distal histidine and the ligands. In order to account for the influence of the protein environment, we compared the ML bond strengths in the proteins with those of corresponding gas phase models. Sketches of the active sites of Fe(III)Mb, Mn (III)Mb and Co(III)Mb with the four ligands as well the corresponding active site gas phase models, investigated in this work, are presented in Fig. 1. As revealed in Fig. 1, in the six of the investigated protein systems the ligand forms either an

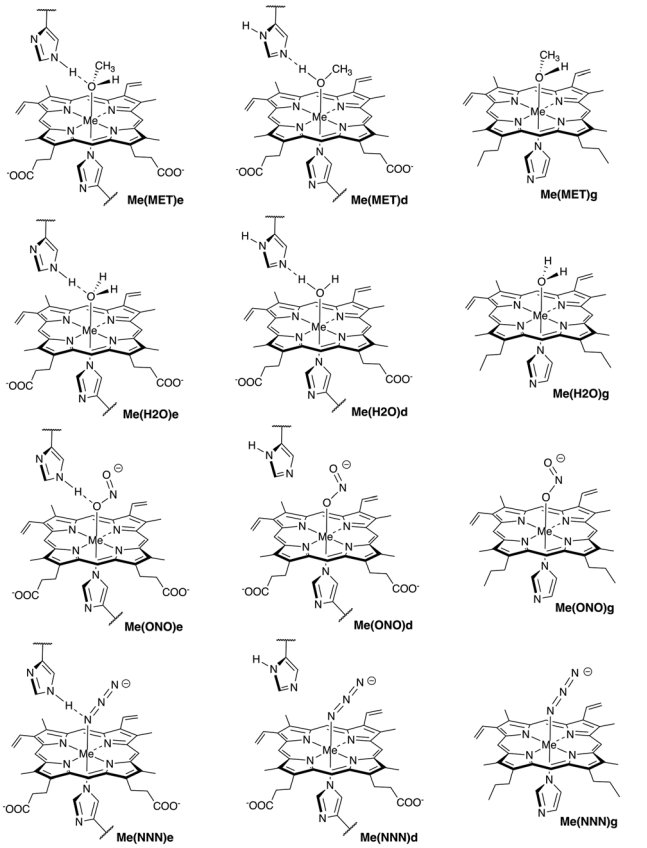

Fig. 1 Sketches of active sites in Mb and gas phase models with ligands investigated in this study (Me = Fe, Mn, and Co). Symbols "e" and "d" indicate distal histidine in ε and δ protonation forms, respectively, while symbol "g" indicates gas phase models. For molecular labels, see text.

O···H or an N ···H HB with the distal histidine, which we compared with the corresponding HB strengths in the water dimer (**H_2OHOH**) and the water–ammonia pair (**HOHNH_3**). Two tautomeric forms of distal histidine were considered, namely His64ε and His64δ (labeled in the following as "e" and "d"), which led to 24 protein complexes and 12 gas phase models. A special focus of this work was on exploring the relevance of the strength of these ML/HB interactions regarding catalytic activity or function of these Mbs for neutral *versus* ionic ligands as well as for Co and Mn substituted Fe-heme co-factors.

The following complex notation is used throughout the manuscript (see also Fig. 1): (i) iron complexes: **Fe(MET)e**, **Fe(MET)d**, **Fe(H_2O)e**, **Fe(H_2O)d**, **Fe(ONO)e**, **Fe(ONO)d**, **Fe(NNN)e**, and **Fe(NNN)d**; (ii) manganese complexes: **Mn(MET)e**, **Mn(MET)d**, **Mn(H_2O)e**, **Mn(H_2O)d**, **Mn(ONO)e**, **Mn(ONO)d**, **Mn(NNN)e**, and **Mn(NNN)d**; (iii) cobalt complexes: **Co(MET)e**, **Co(MET)d**, **Co(H_2O)e**, **Co(H_2O)d**, **Co(ONO)e**, **Co(ONO)d**, **Co(NNN)e**, and **Co(NNN)d**; (iv) corresponding heme co-factor ligand gas phase models: **Fe(MET)g**, **Fe(H_2O)g**, **Fe(ONO)g**, and **Fe(NNN)g**; **Mn(MET)g**, **Mn(H_2O)g**, **Mn(ONO)g**, and **Mn(NNN)g**; and **Co(MET)g**, **Co(H_2O)g**, **Co(ONO)g**, and **Co(NNN)g**. We utilized for the protein calculations a hybrid QM/MM (quantum

mechanics – molecular mechanics) ansatz,[44–48] and for the bond strength assessment we used the local vibrational mode theory (LMA) developed in our group,[49,50] complemented with Bader's quantum theory of atoms in molecules (QTAIM) analysis[51–53] and natural bond orbital (NBO) analysis.[54,55]

2 Materials and methods

2.1 Local vibrational mode analysis

In order to assess and compare ML and HB in the Mb complexes investigated in this work a qualified bond strength descriptor is needed. One popular measure to assess bond strength is to use normal mode stretching force constants derived from a normal mode analysis.[56] However, as pointed out by Wilson in his pioneering 1941 publication[57] normal vibrational modes of polyatomic molecules are generally delocalized, limiting this approach. LMA[49,50] originally developed by Konkoli and Cremer[58,59] has solved this problem *via* extracting local vibrational modes and corresponding local mode force constant from the normal vibrational modes.

A local vibrational mode $\mathbf{a}_n$ is defined as

$$\mathbf{a}_n = \frac{\mathbf{K}^{-1}\mathbf{d}_n{}^{\dagger}}{\mathbf{d}_n\mathbf{K}^{-1}\mathbf{d}_n{}^{\dagger}} \quad (1)$$

The two ingredients needed for LMA, the diagonal normal mode force constant matrix $\mathbf{K}$ in normal mode coordinates $\mathbf{Q}$ and the normal mode vectors $\mathbf{d}_n$ in internal coordinates, can be obtained from a vibrational frequency calculation *via* the Wilson GF formalism,[60,61] which is a routine part of most modern quantum chemistry packages.[62] As a consequence, LMA can be applied with minimal computational costs after a routine quantum-chemical calculation of vibrational frequencies, optionally adding measured frequencies as input (a feature opening LMA to the experimental vibrational spectroscopists) to both single molecules in gas phase, solution, or in a protein, but also to periodic systems and crystals.[49,50]

For each local mode $\mathbf{a}_n$, one can derive associated local force constants k_n^a describing the local vibration of the atomic fragment under consideration,

$$k_n^a = \mathbf{a}_n{}^{\dagger}\mathbf{K}\mathbf{a}_n = \frac{1}{\mathbf{d}_n\mathbf{K}^{-1}\mathbf{d}_n{}^{\dagger}} \quad (2)$$

local mode frequencies, local mode infrared intensities and other local properties can be determined.[50,63]

Over the past two decades, we have successfully applied local mode force constants to characterize the strength of covalent bonds and non-covalent interactions across the periodic table as documented in two recent review articles,[49,50] including bonding inside the active sites of hemoproteins.[64–71] Another important feature of LMA is the characterization of normal mode (CNM) procedure, which decomposes each normal vibrational mode into local mode contributions.[49,50,72,73] CNM has advanced the interpretation of vibrational spectra to the next level *e.g.*, identifying which molecular fragments couple in DNA–base pairs or assessing the quality of Stark effect probes with a local probe bond, just to name two examples.[67,74–76] A detailed description of the underlying local vibrational mode theory can also be found in the two review articles.[49,50]

In this work we predominantly focused on local mode stretching force constants k^a(AB) reflecting the intrinsic strength the bond/weak interaction between two atoms A and B,[77] applied to ML and ligand–histidine HB. For easier comparison we transformed the local mode force constants k^a(AB) into relative bond strength orders (BSO) according to the generalized Badger rule derived by Cremer, Kraka, and coworkers[78,79] *via* a power relationship in the form of BSO = $x(k^a)^y$. Two reference molecules with known BSO and force constants are utilized to obtain the parameters for x and y, with the constraint that a zero value for the force constant k^a(AB) equals a zero BSO value. The reference molecules utilized in our study are presented in Table 1. For the Me–ligand bonds we referred to Mayer's bond orders[80–82] instead of using BSO = 1 for single and BSO = 2 for double bonds, which in past studies involving transition metal bonding have turned out to be a better choice.[49,50,64,68,83]

We complemented LMA with features of the analysis of the electron density $\rho(\mathbf{r})$ *via* Bader's QTAIM theory.[51–53] In particular the covalent character of the ML and HBs were determined *via* the Cremer–Kraka criterion,[84,85] which is based on the local electron density $H(\mathbf{r}) = G(\mathbf{r}) + V(\mathbf{r})$, where the kinetic energy density is $G(\mathbf{r})$ (positive, destabilizing) and the potential energy density is $V(\mathbf{r})$ (negative, stabilizing). If at the bond critical point $\mathbf{r}_b$ of $\rho(\mathbf{r})$ between two bonded atoms AB $H(\mathbf{r}_b)$ is negative, the character of AB bond is predominantly covalent, whereas a positive $H(\mathbf{r}_b)$ value indicates a predominantly electrostatic character. In addition we analyzed the atomic NBO charges in ML and HB.[54,86]

2.2 Calculational details

The starting geometries for the Mn(III)Mb protein systems with methanol (CH_3OH), water (H_2O), nitrite (NO_2^-), and azide (N_3^-) ligands placed in the distal heme pocket (see Fig. 1) were taken from the horse heart X-ray structures of oxidized manganese substituted myomoglobin with methanol (PDB entry: 2O5L), water (PDB entry: 2O58), nitrite (PDB entry: 2O5O), and

Table 1 Bond length R, local mode force constant k^a, and bond strength order BSO of selected bonds in reference molecules used in our study

Bond	R (Å)	k^a (mDyn Å^{-1})	BSO[a]	Molecule
Me–C	1.792	3.243	1.005	$CuCH_3$
Me═C	1.641	5.568	1.894	$NiCH_2$
N–H, O–H	1.142	1.340	0.500	F_2H^-
	0.920	9.804	1.000	FH

[a] BSO values of bonds involving metal atoms are based on Mayer's bond orders.[80–82]

azide (PDB entry: 2O5 M) ligands in the heme distal pocket.[18] The starting geometries for the Fe(III)Mb and Co(III)Mb protein systems were obtained from the corresponding Mn(III)Mb complexes by manually substituting the Mn metal center with Fe and Co, respectively. For all eight complexes hydrogen atoms were added to the experimental protein structures and the proteins were neutralized by counter-ions using AMBER.[87] In order to simulate a water environment, the active sites of the proteins were surrounded by a sphere of TIP3P water molecules,[88] with a radius of 16 Å. After initial minimization with AMBER, the protein systems were divided into a QM part including the heme co-factor, distal and proximal histidine side chains of Mb, and the ligand (*ca.* 110 atoms), while the MM part included remaining protein atoms (*ca.* 3000 atoms) as well as water molecules. Based on previous work on Mb[64,68] and supported by the finding of others reporting that the PBE0 functional[89,90] shows good performance for the calculation of transition metals complexes,[91–94] we used for the QM/MM calculations PBE0 in combination with Pople's 6-31G(d,p) basis set.[95] For the MM part we applied the AMBER fore field.[87] The QM/MM geometry optimization and frequency calculations were performed with scaled electronic embedding using the ONIOM method.[96] All QM/MM geometry optimizations finished as local minima on the potential energy surface, *i.e.*, no imaginary normal mode frequencies were found. The calculations in the gas phase were done in this study using the PBE0/6-31G(d,p) level of theory. Using this model chemistry, the calculated FeN bond length of 1.965 Å in the ferric state turned out to be close to the X-ray bond length in bis(1-methylimidazole) (*meso*-tetramesitylporphinato) Fe(III) (1.970 Å).[97]

Our previous calculations on Fe(III)Mb systems[68] in line with experimental data on an Fe(III)Mb–water ligand complex[98,99] suggest that the heme co-factor is a high-spin species. Therefore, we calculated Fe(III)Mb complexes with the neutral ligands (*i.e.*, water and methanol) in their quartet electronic state (S = 3/2). In contrast, experimental data on Fe(III) Mb complexes with ionic ligands (*i.e.*, nitrite and azide) suggest a low-spin heme co-factor.[100–102] Following this suggestion, we calculated Fe(III)Mb complexes with the nitrite and azide ligands in their doublet electronic state (S = 1/2). Similarly, following suggestions based on experimental data, the Mn(III)Mb protein systems were calculated in this study as high-spin species (S = 2),[23,103] and Co(III)Mb protein systems as low-spin species (S = 0).[32] Geometry optimizations and vibrational frequency calculations were performed with Gaussian16,[104] the LMA analysis was performed using our LModeA program.[105] The QTAIM analysis was performed with the AIMALL program[106] and NBO charges were calculated utilizing the NBO analysis implemented in Gaussian16. In the following, we present the results of our calculations to three decimal places for most bond properties investigated in this study. To justify this level of accuracy, we performed calculations for **Fe(MET)e** and **Fe(MET)d** using the B3LYP/6-311G(d,p)/AMBER level of theory, and a comparison with the PBE0/6-31G(d,p)/AMBER method is provided in Table S1 on page S4 of the ESI.† Additionally, we compared the PBE0/6-31G(d,p)/AMBER level of theory with PBE0/def2-TZVP/SDD(Fe)/AMBER, and the results are presented in Table S7 on page S5 of the ESI.† Table S2 on page S4 of the ESI† shows a comparison of theoretical bond lengths for the heme group in **Mn(MET)e** and **Mn(MET)d** with experimental data (PDB entry: 2O5L). Moreover, Tables S3 and S4 on page S5 of the ESI† show the results of calculations for **Fe(MET)e** and **Fe(MET)d** using the PBE0/6-31G(d,p)/AMBER level of theory in the doublet, quartet, and sextet electronic states.

3 Results and discussion

In the following ML bonding is discussed for the Fe(III)Mb–ligand complexes and their gas phase analogues, followed by Mn(III)Mb–ligand bonding and Co(III)Mb–ligand bonding. In addition to forming chemical bonds with the metal of the heme cofactor, there is also the opportunity for HB formation with the distal histidine for six protein ligand complexes, as shown in Fig. 1. This will be elucidated in the following sections for the Fe, Co, and Mn protein complexes.

3.1 ML bonds in Fe(III)Mb

Fe–ligand bond properties of the investigated Fe(III)Mb–ligand complexes and the corresponding gas phase models are presented in Table 2. Relationships between these properties are shown in Fig. 2 and 3.

According to Fig. 2a, the Fe–ligand bond strength clusters into two groups; one group for systems with the two neutral ligands, methanol (**Fe(MET)e**, **Fe(MET)d**, and **Fe(MET)g**, with an average k^a value of 0.680 mDyn Å^{-1}) and water (**Fe(H_2O)e**, **Fe(H_2O)d**, and **Fe(H_2O)g**, with an average k^a value of 0.635 mDyn Å^{-1}). The other group is involving the two ionic ligands, nitrite (**Fe(ONO)e**, **Fe(ONO)d**, and **Fe(ONO)g**, with an average k^a value of 2.241 mDyn Å^{-1}) and azide (**Fe(NNN)e**, **Fe(NNN)d**, and **Fe(NNN)g**, with an average k^a value of 2.105 mDyn Å^{-1}). Overall, ionic ligands are characterized by

Table 2 Bond length R, local mode force constant k^a, energy density at bond critical point H_{ρ}, charge difference Δq, and bond strength order BSO of ML bonds in Fe(III)Mb proteins along with gas phase models investigated in our study; for molecular labels, see text

Molecule	Bond	R (Å)	k^a (mDyn Å^{-1})	H_ρ (Hr Bohr^{-3})	Δq (e)	BSO
Fe(MET)e	FeO	2.398	0.270	−0.0059	2.194	0.055
Fe(MET)d	FeO	2.140	0.679	−0.0062	2.257	0.161
Fe(ONO)e	FeO	1.881	2.020	−0.0082	1.691	0.577
Fe(ONO)d	FeO	1.852	2.310	−0.0141	1.627	0.675
Fe(H_2O)e	FeO	2.409	0.257	−0.0054	2.218	0.051
Fe(H_2O)d	FeO	2.184	0.608	−0.0068	2.400	0.141
Fe(NNN)e	FeN	1.911	1.953	−0.0232	1.671	0.555
Fe(NNN)d	FeN	1.875	2.237	−0.0322	1.557	0.650
Fe(MET)g	FeO	1.992	1.091	0.0023	1.942	0.280
Fe(ONO)g	FeO	1.846	2.392	−0.0146	1.629	0.703
Fe(H_2O)g	FeO	2.010	1.039	0.0030	2.084	0.265
Fe(NNN)g	FeN	1.884	2.125	−0.0277	1.546	0.612

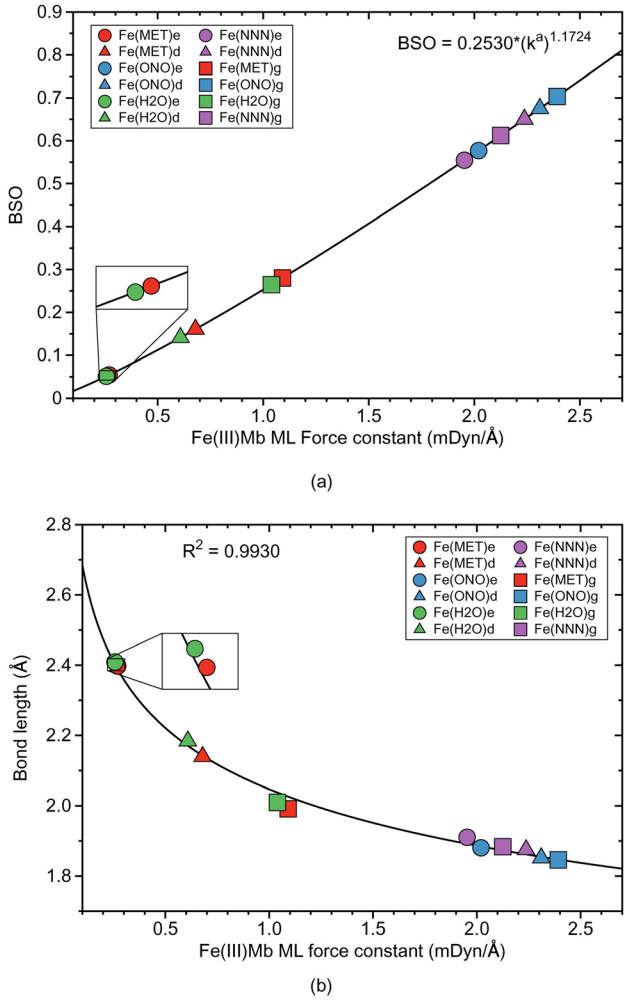

Fig. 2 Properties of ML bonds in Fe(III)Mb complexes and corresponding gas phase models. (a) Bond strength order BSO calculated from local mode force constants k^a *via* the generalized Badger rule. (b) Relation between local mode force constant k^a and bond length R. For molecular labels, see text.

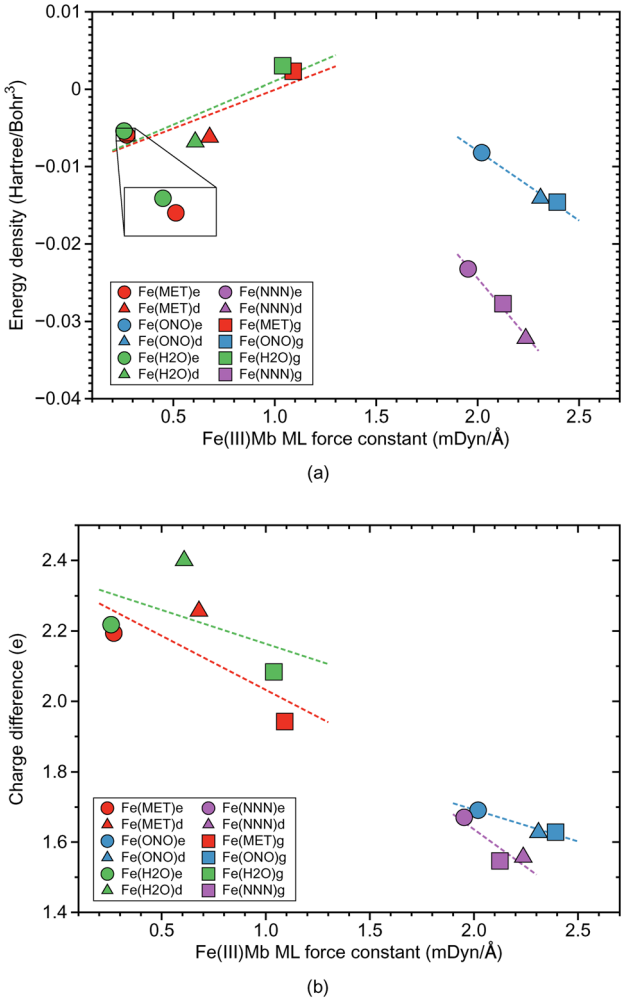

Fig. 3 Properties of ML bonds in Fe(III)Mb complexes and corresponding gas phase models. (a) Relation between local mode force constant k^a and energy density H_ρ. (b) Relation between local mode force constant k^a and atomic charge difference. For molecular labels, see text.

considerably stronger Fe–ligand bonding with BSO values between 0.6 and 0.7, whereas as neutral ligands lead to weak Fe–ligand bonds with BSO values in the range of 0.05–0.25. Interesting to note is that for ionic ligands BSO values for proteins and gas phase reference Fe–ligand bonds are comparable whereas for neutral ligands gas phase values are at the stronger end. Moreover, the strength of the Fe–ligand bond in the proteins for the ε protonation form is smaller than for the δ protonation form.

Fig. 2b shows the relationship between the local mode force constant k^a and the bond length R for the molecular systems involving the Fe–ligand chemical bond. According to this figure the stronger bond generally correlates well (R^2 = 0.9930) with the smaller bond length, which is consistent with the Badger rule.[79,107] The covalent character of this bond is expressed in our study by the energy density at the bond critical point H_ρ, where the more negative value of the energy density indicates on a more covalent bond character. The relation between those two quantities is presented in Fig. 3a. We find three clusters formed by the individual ligands investigated in this study. The average energy density for the molecular systems with methanol has an H_ρ value of −0.0032 Hartree per Bohr^3, which indicates on a small covalent character of this bond, similarly as for the molecular systems with water where the average energy density has an H_ρ value of −0.0031 Hartree per Bohr^3. The Fe–ligand chemical bond has more pronounced covalent character for the molecular systems with the ionic ligands. The average energy density for the molecular systems with nitrite has an H_ρ value of −0.0123 Hartree per Bohr^3, while for the systems with azide it has an H_ρ value of −0.0277 Hartree per Bohr^3. Fig. 3b shows the relation between the local mode force constant k^a and the charge difference Δq between the Fe atomic charge and the O or N atomic charge of the ligand. Similar as in Fig. 3a, we find three clusters in Fig. 3b formed by the individual ligands. Larger charge differences are observed for molecular systems

with water (an average Δq value of 2.234 e) and with methanol (an average Δq value of 2.131 e), and smaller for systems with nitrite (an average Δq value of 1.649 e) and azide (an average Δq value of 1.591 e).

3.2 ML bonds in Mn(III)Mb

ML bond properties of the Mn(III)Mb–ligand complexes and the corresponding gas phase models are presented in Table 3. Relationships between these properties are shown in Fig. 4 and 5.

According to Fig. 4a, the Mn–ligand bonds cluster into two groups, one with neutral ligands and one with ionic ligands. The molecular systems with the water ligand have an average force constant k^a of 0.354 mDyn Å^{-1}. Similarly as for systems with Fe–ligand bonds, the strength of the Mn–ligand bond in the protein is smaller for the ε protonation form of distal histidine than in the δ form. The strength of the Mn–ligand bond in the systems with methanol is widely distributed keeping a small value for the gas phase model (k^a of a value of 0.365 mDyn Å^{-1}), through a medium value for the ε protein system (k^a of a value of 0.949 mDyn Å^{-1}), to a relatively big value for the δ protein system (k^a of a value of 1.612 mDyn Å^{-1}). Both molecular systems with the ionic ligands have a medium strength, with the average value of the force constant k^a of a value of 1.062 mDyn Å^{-1} for the system with nitrite, and a value of 1.138 mDyn Å^{-1} for the system with azide. However, the average strength of the Mn–ligand bonds (k^a of a value of 0.882 mDyn Å^{-1}), is smaller than the average strength of the Fe–ligand bonds (k^a of a value of 1.415 mDyn Å^{-1}). For the neutral ligands forming the bond with Mn, the BSO values range between 0.05 and 0.1, and the BSO values for the ionic ligands are in the range of 0.2–0.45, *i.e.*, they show a larger spread than their Fe–ligand counterpart. According to Fig. 4b, the local mode force constant k^a of the Mn–ligand bond relatively good correlates (R^2 = 0.9897) with the bond length R, and according to Fig. 5a, the Mn–ligand bonds in all systems have a covalent character, confirmed by negative values of the energy density (an average H_ρ value of −0.0047, −0.0040, and −0.0108 Hartree per Bohr^3, for the systems with water, nitrite, and azide, respectively), with one exception. The Mn–ligand bond shows electrostatic character for the δ protein system with methanol (H_ρ of a value of 0.0010 Hartree per Bohr^3), which is also the strongest Mn–ligand bond (k^a of a value of 1.612 mDyn Å^{-1}). According to Fig. 5b, the largest atomic charge difference of the Mn–ligand bond is observed in our calculations for molecular systems with water (an average Δq value of 2.503 e), and the smallest values are observed for both systems with the ionic ligands (the average Δq value of 2.105 and 2.068 e, for the system with nitrite and azide, respectively). The charge difference for the system with methanol has a medium value (an average Δq value of 2.304 e).

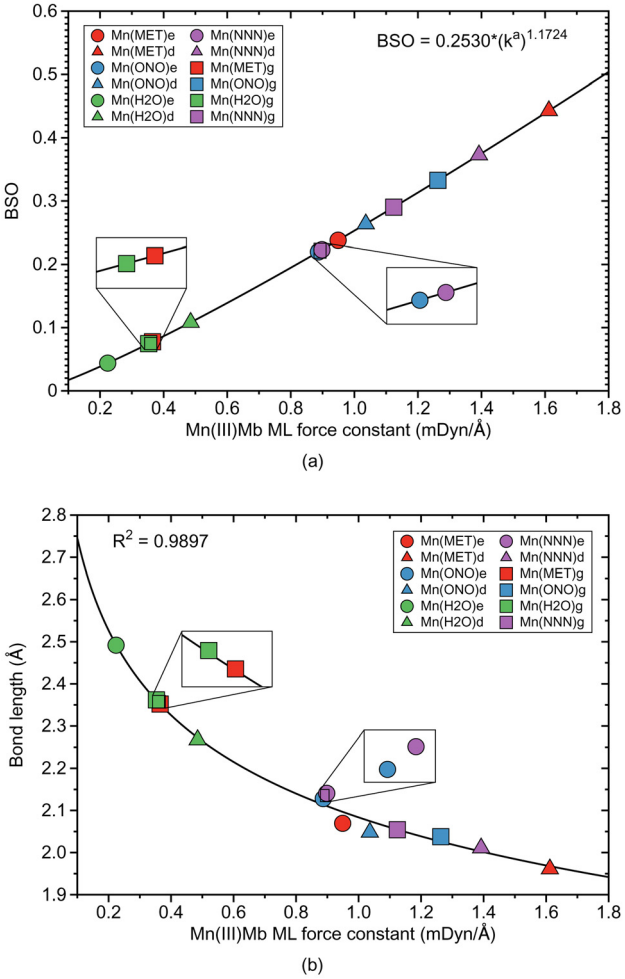

Fig. 4 Properties of ML bonds in Mn(III)Mb–ligand complexes and corresponding gas phase models. (a) Bond strength order BSO calculated from local mode force constants k^a *via* the generalized Badger rule. (b) relation between local mode force constant k^a and bond length R. For molecular labels, see text.

Table 3 Bond length R, local mode force constant k^a, energy density at bond critical bond H_ρ, charge difference Δq, and bond strength order BSO of ML bonds in Mn(III)Mb proteins along with gas phase models investigated in our study; for molecular labels, see text

Molecule	Bond	R (Å)	k^a (mDyn Å^{-1})	H_ρ (Hr Bohr^{-3})	Δq (e)	BSO
Mn(MET)e	MnO	2.070	0.949	−0.0029	2.272	0.238
Mn(MET)d	MnO	1.961	1.612	0.0010	2.322	0.443
Mn(ONO)e	MnO	2.128	0.887	−0.0042	2.131	0.220
Mn(ONO)d	MnO	2.048	1.036	−0.0032	2.084	0.264
Mn(H_2O)e	MnO	2.492	0.224	−0.0047	2.492	0.044
Mn(H_2O)d	MnO	2.268	0.485	−0.0046	2.532	0.108
Mn(NNN)e	MnN	2.141	0.898	−0.0100	2.144	0.223
Mn(NNN)d	MnN	2.011	1.392	−0.0103	2.014	0.373
Mn(MET)g	MnO	2.352	0.365	−0.0051	2.317	0.078
Mn(ONO)g	MnO	2.038	1.263	−0.0047	2.099	0.333
Mn(H_2O)g	MnO	2.362	0.353	−0.0049	2.485	0.075
Mn(NNN)g	MnN	2.054	1.124	−0.0122	2.046	0.290

3.3 ML bonds in Co(III)Mb

Co–ligand bond properties of the Co(III)Mb–ligand complexes and the corresponding gas phase models are presented in Table 4. Relationships between these properties are shown in

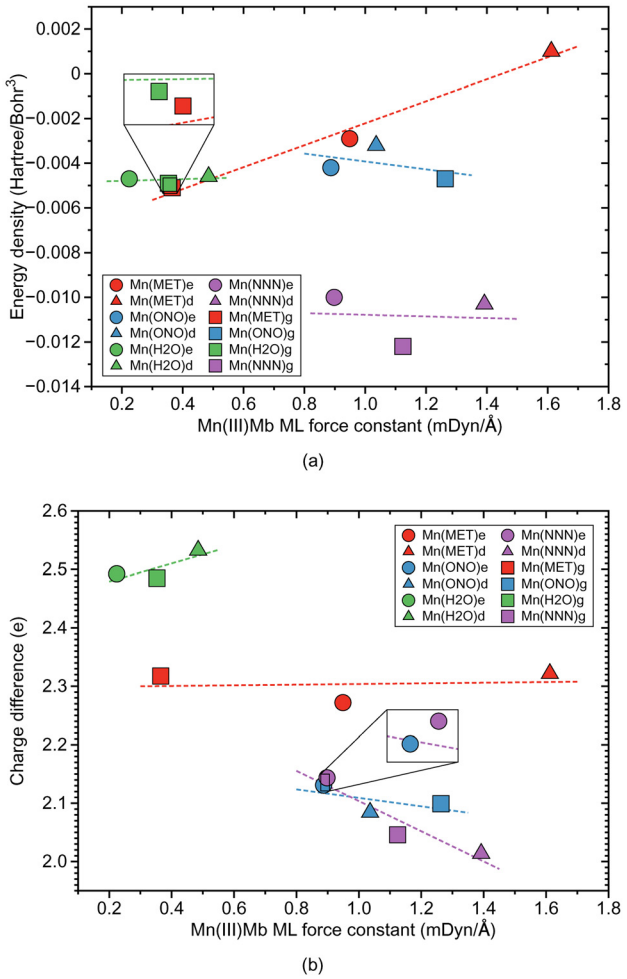

Fig. 5 Properties of ML bond in Mn(III)Mb–ligand complexes and corresponding gas phase models. (a) Relation between local mode force constant k^a and energy density H_ρ. (b) Relation between local mode force constant k^a and atomic charge difference. For molecular labels, see text.

Table 4 Bond length R, local mode force constant k^a, energy density at bond critical bond H_ρ, charge difference Δq, and bond strength order BSO of ML bonds in Co(III)Mb–ligand complexes along with the corresponding gas phase models investigated in our study; for molecular labels, see text

Molecule	Bond	R (Å)	k^a (mDyn Å^{-1})	H_ρ (Hr Bohr^{-3})	Δq (e)	BSO
Co(MET)e	CoO	2.020	0.908	−0.0017	1.789	0.226
Co(MET)d	CoO	1.934	1.656	−0.0005	1.834	0.457
Co(ONO)e	CoO	1.878	2.102	−0.0097	1.508	0.605
Co(ONO)d	CoO	1.856	2.381	−0.0148	1.448	0.700
Co(H_2O)e	CoO	2.008	0.970	0.0005	1.924	0.244
Co(H_2O)d	CoO	1.937	1.574	−0.0007	1.943	0.431
Co(NNN)e	CoN	1.914	1.971	−0.0254	1.489	0.561
Co(NNN)d	CoN	1.892	2.170	−0.0316	1.367	0.628
Co(MET)g	CoO	1.975	1.254	0.0003	1.738	0.330
Co(ONO)g	CoO	1.855	2.412	−0.0147	1.438	0.710
Co(H_2O)g	CoO	1.975	1.242	0.0008	1.868	0.326
Co(NNN)g	CoN	1.902	2.047	−0.0297	1.371	0.586

Fig. 6 and 7. According to Fig. 6a, the Co–ligand bond strengths can be grouped into two clusters, one representing the weaker neutral Co–ligand bonds and one with the stronger Co–ligand ionic bonds, *i.e.*, we find the same trends as for the Fe and Mn systems. The Co–ligand bond strength for the systems with the neutral ligands is substantially smaller (average k^a value of 1.262 and 1.273 mDyn Å^{-1}, for water and methanol, respectively) than for the systems with the ionic ligands (average k^a value of 2.298 and 2.063 mDyn Å^{-1}, for nitrite and azide, respectively). However, in contrast to the Fe–ligand bonds, we find a larger spread for the neutral system with the BSO range between 0.2–0.45 for the neutral ligands, and 0.5–0.7 for the ionic ligands, respectively. Similarly as in the Fe–ligand bonds, the strength of the Co–ligand bond in the ε protein conformer is smaller than that in the δ conformer. Overall, the average strength of the Co–ligand bonds (average k^a of a value of 1.724 mDyn Å^{-1}) is larger than the

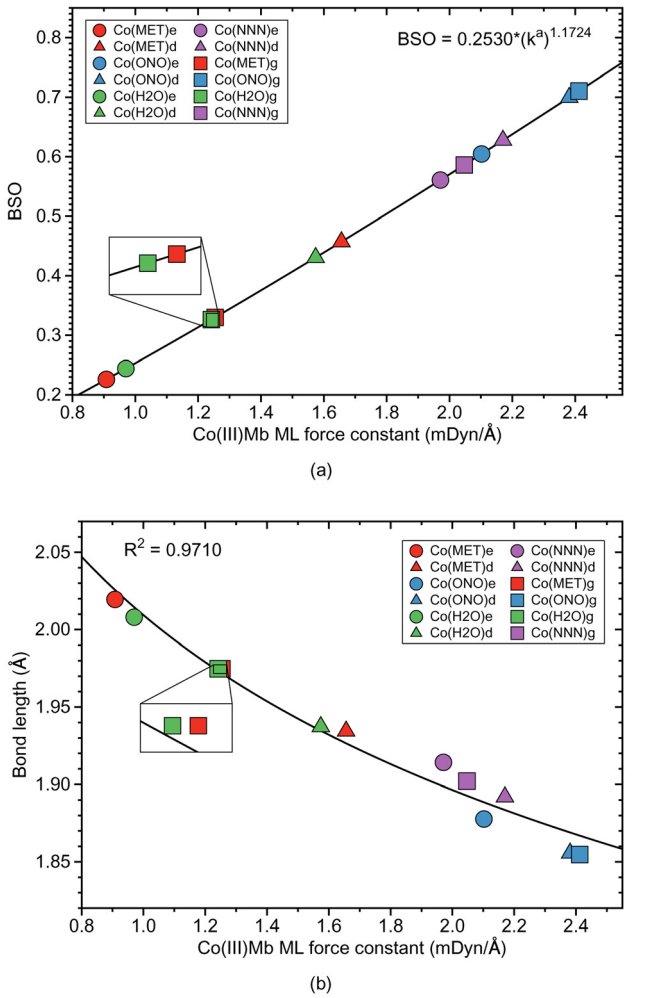

Fig. 6 Properties of ML bonds in Co(III)Mb–ligand complexes and corresponding gas phase models. (a) Bond strength order BSO calculated from local mode force constants k^a *via* the generalized Badger rule. (b) Relation between local mode force constant k^a and bond length R. For molecular labels, see text.

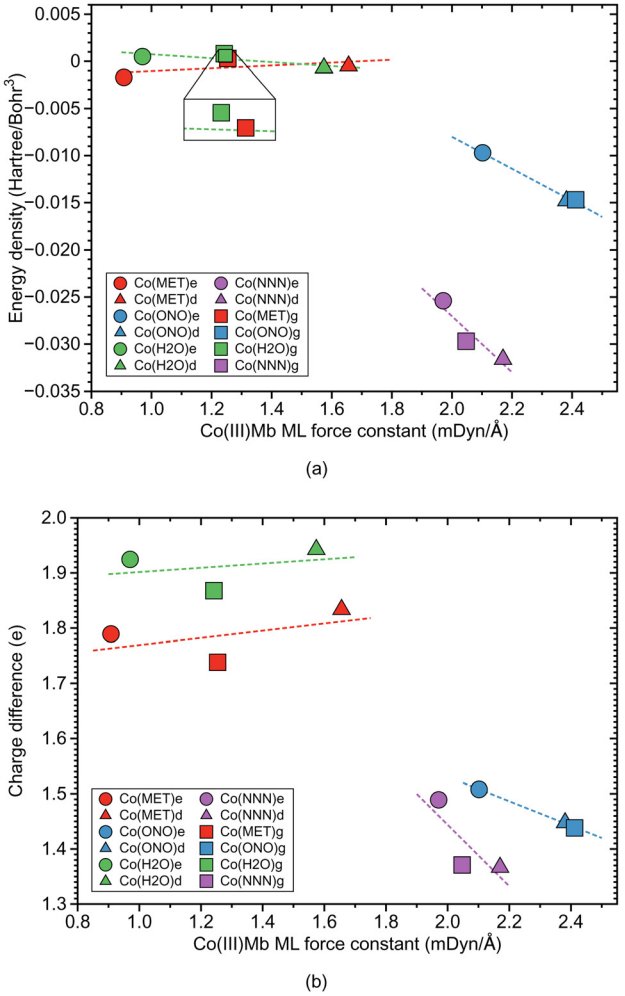

Fig. 7 Properties of ML bonds in Co(III)Mb–ligand complexes and corresponding gas phase models. (a) Relation between local mode force constant k^a and energy density H_ρ. (b) Relation between local mode force constant k^a and atomic charge difference. For molecular labels, see text.

average strength of the Fe–ligand bonds (average k^a of a value of 1.415 mDyn Å^{-1}) and that of the Mn–ligand bonds (average k^a of a value of 0.882 mDyn Å^{-1}).

According to Fig. 6b, Co–ligand local mode force constants k^a correlate well correlates with the Co–ligand bond lengths R (R^2 = 0.9710). Fig. 7a reveals that, similarly as found for the Fe systems, the neutral Co–ligand bonds have an energy density H_ρ which is close to zero (an average H_ρ value of 0.0002 and −0.0006 Hartree per Bohr^3, for water and methanol, respectively), indicating on a predominant electrostatic character of this bond. However, the systems with the ionic Co–ligand bonds display a covalent character (average H_ρ value of −0.0131 and −0.0289 Hartree per Bohr^3, for nitrite and azide, respectively). As shown in Fig. 7b, we find a similar relationship between the atomic charge difference Δq and the local mode force constant k^a for the Co–ligand bonds as for the systems involving the Fe–ligand bonds. The charge difference between the Co and ligand atoms for the neutral ligands is relatively big (average Δq value of 1.912 and 1.787 e, for water and methanol, respectively), when compared to the charge differences for the systems involving the ionic ligands (average Δq value of 1.465 and 1.409 e, for nitrite and azide, respectively).

3.4 Protein–ligand hydrogen bonding

As depicted in Fig. 1, in six of the investigated Mb–ligand complexes, the ligand can form a HB with the distal histidine, namely in **Me(MET)e**, **Me(MET)d**, **Me(H_2O)e**, **Me(H_2O)d**, **Me(ONO)e**, and **Me(NNN)e**. The ε form of the distal histidine serves as HB donor leading to O···H type HBs with the ligand for **Me(MET)e**, **Me(H_2O)e**, and **Me(ONO)e**, and for **Me(NNN)e** to an N···H type HB. The δ form of the distal histidine serves as HB acceptor leading to N···H type HBs with the ligand for **Me(MET)d** and **Me(H_2O)d**.

Table 5 shows HB properties for the MeMb–ligand complexes (Me = Fe, Mn, Co) along with HB properties of the water dimer (**H_2OHOH**) and the water–ammonia pair (**$HOHNH_3$**, where water is a hydrogen atom donor) for comparison. Fig. 8, 9, and 10 show HB BSO values calculated from local mode force constants k^a *via* the generalized Badger rule, and the relationship between local mode HB force constant k^a and bond length R. The corresponding relationships between HB force constant k^a and energy density H_ρ, as well as between HB force constant k^a and the atomic charge difference between the two atoms engaged in the HB, are presented in Fig. S1–S3 of the ESI.† In the following HBs for the Fe(III)Mb, Mn(III)Mb, and Co(III)Mb–ligand complexes are discussed, followed by the CNM analysis comparing ε and δ hydrogen bonding.

Table 5 Bond length R, local mode force constant k^a, energy density at bond critical bond H_ρ, charge difference Δq, and bond strength order BSO of protein–ligand HBs in Fe(III)Mb, Mn(III)Mb, and Co(III)Mb–ligand complexes and the water dimer and water–ammonia pair reference systems; for molecular labels, see text

Molecule	Bond	R (Å)	k^a (mDyn Å^{-1})	H_ρ (Hr Bohr^{-3})	Δq (e)	BSO
Fe(MET)e	O···H	2.074	0.127	−0.0008	1.223	0.220
Fe(MET)d	N···H	1.620	0.386	−0.0118	1.111	0.324
Fe(ONO)e	O···H	2.195	0.106	−0.0006	0.994	0.207
Fe(H_2O)e	O···H	2.094	0.109	−0.0006	1.421	0.209
Fe(H_2O)d	N···H	1.726	0.293	−0.0037	1.103	0.294
Fe(NNN)e	N···H	1.850	0.298	−0.0011	1.018	0.296
Mn(MET)e	O···H	2.174	0.114	−0.0004	1.235	0.212
Mn(MET)d	N···H	1.559	0.346	−0.0210	1.117	0.312
Mn(ONO)e	O···H	1.952	0.180	−0.0014	1.091	0.248
Mn(H_2O)e	O···H	2.134	0.081	−0.0004	1.421	0.188
Mn(H_2O)d	N···H	1.743	0.251	−0.0035	1.112	0.279
Mn(NNN)e	N···H	1.744	0.356	−0.0033	1.123	0.315
Co(MET)e	O···H	2.169	0.141	−0.0004	1.170	0.228
Co(MET)d	N···H	1.605	0.343	−0.0141	1.121	0.311
Co(ONO)e	O···H	2.159	0.118	−0.0007	0.962	0.215
Co(H_2O)e	O···H	2.251	0.051	0.0001	1.346	0.160
Co(H_2O)d	N···H	1.684	0.280	−0.0063	1.114	0.290
Co(NNN)e	N···H	1.827	0.312	−0.0014	0.993	0.301
H_2 OHOH	O···H	1.906	0.214	−0.0013	1.446	0.264
$HOHNH_3$	N···H	1.917	0.239	−0.0016	1.657	0.274

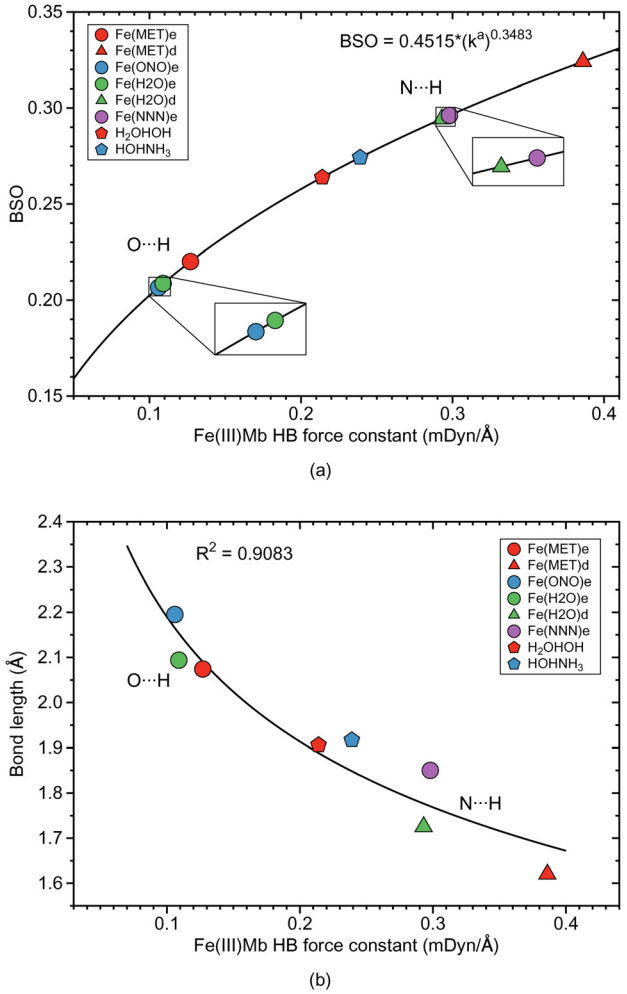

Fig. 8 HB properties of Fe(III)Mb–ligand complexes and corresponding properties of the water and water–ammonia molecular complexes. (a) Bond strength order BSO calculated from local mode force constants k^a *via* the generalized Badger rule. (b) Relation between local mode force constant k^a and bond length R. For molecular labels, see text.

3.4.1 HBs in Fe(III)Mb. According to Fig. 8a and Table 5, the weakest HBs for the Fe(III)Mb–ligand complexes are observed for **Fe(MET)e**, **Fe(H_2O)e**, and **Fe(ONO)e** (average k^a value of 0.114 mDyn Å^{-1}) which are HBs of O···H type involving the ε form of distal histidine. For **Fe(MET)e** and **Fe(H_2O)e** the weak HBs are paired with weak Fe–ligand bonds (average k^a value of 0.162 mDyn Å^{-1}). That is not the case for **Fe(ONO)e**, where the ionic ONO ligand forms a strong Fe–ligand bond (k^a value of 2.020 mDyn Å^{-1}). The strongest HBs (average k^a value of 0.340 mDyn Å^{-1}) are found for **Fe(MET)d** and **Fe(H_2O)d**. They are of N···H type involving the δ form of distal histidine and are paired with only medium strong Fe–ligand bonds. The HB in **Fe(NNN)e** is relatively strong (k^a value of 0.298 mDyn Å^{-1}), paired with a relatively strong Fe–ligand bond. The findings suggest that there is no obvious correlation between the HB and the ML bond strengths. However, we observe a general trend that the N···H type HBs involving δ histidine are stronger than O···H type HBs involving ε histidine. The same is observed for the HBs in the gas phase molecular complexes, where according to Table 5, the water dimer (**H_2OHOH**) with the O atom acting as a hydrogen acceptor (k^a value of 0.214 mDyn Å^{-1}) has a weaker HB weaker than the water–ammonia pair (**HOHNH_3**) with the N atom acting as an acceptor (k^a value of 0.239 mDyn Å^{-1}). Interesting to note is also that the O···H type HBs of the protein are considerably weaker than the HB of the water dimer in the gas phase. In contrast, the N···H type HBs of the protein are stronger than the corresponding HB of the water–ammonia pair in the gas phase, indicating on the influence of both the transition metal and the protein environment on the HB strength.

According the Fig. S1a of the ESI,† the weak O···H type HBs in **Fe(MET)e**, **Fe(H_2O)e**, and **Fe(ONO)e**, exhibit on small covalent character as indicated by their small negative energy density values. On the other hand, the strong N···H type HBs of **Fe(MET)d** and **Fe(H_2O)d**, have more negative energy density values, disclosing more covalent bond character. It is interesting to note that the covalent character of the gas phase reference molecules (**H_2OHOH** and **HOHNH_3**), is relatively small, which indicates on a predominant effect of the protein environment, increasing the covalent character of the N···H type HBs and their strength. According to Fig. 8b, the HB bond strength of the Fe(III)Mb proteins shows a weak correlation with the corresponding HB bond length, with the N···H bonds being overall shorter than their O···H counterparts.

3.4.2 HBs in Mn(III)Mb. HB BSOs as a function of the corresponding local mode force constants k^a s, calculated from the extended Badger relationship (see above), as well the correlation between HB force constants k^a and HB bond length R, for the Mn(III)Mb–ligand complexes are shown in Fig. 9a and b. The correlation between HB force constant k^a and energy density H_ρ, as well as the correlation between k^a and charge difference between the two atoms involved in HB are presented in Fig. S2 of the ESI.†

Overall we observe the same trends as for the Fe(III)Mb–ligand complexes with the following exceptions. As shown in Fig. 9a, weak O···H type HBs are formed between the neutral ligands and the ε form of distal histidine, namely **Mn(MET)e** and **Mn(H_2O)e**. We find the strongest N···H type HB for the ε form of distal histidine with the azide anion (**Mn(NNN)e**). The strongest HBs of N···H type involving the δ form of distal histidine are found for **Mn(MET)d** and **Mn(H_2O)d**. Whereas similar to Fe(III)Mb, the weaker O···H type HB of **Mn(H_2O)e** is paired with a weaker Mn–ligand bond for the ε Mn(III)Mb protein, for **Mn(ONO)e** and **Mn(MET)e** the Mn–ligand bond strength lies in the middle range. The ε form of the Mn(III)Mb protein azide complex (**Mn(NNN)e**) with the strongest N···H type HB in this series is paired with a Mn–ligand bond of middle strength.

3.4.3 HBs in Co(III)Mb. Fig. 10a and b present BSO values as a function of the local mode HB force constants k^a for the Co(III)Mb–ligand complexes, calculated from the extended Badger relationship, and the correlation between the HB force constants k^a and the corresponding bond length R. In

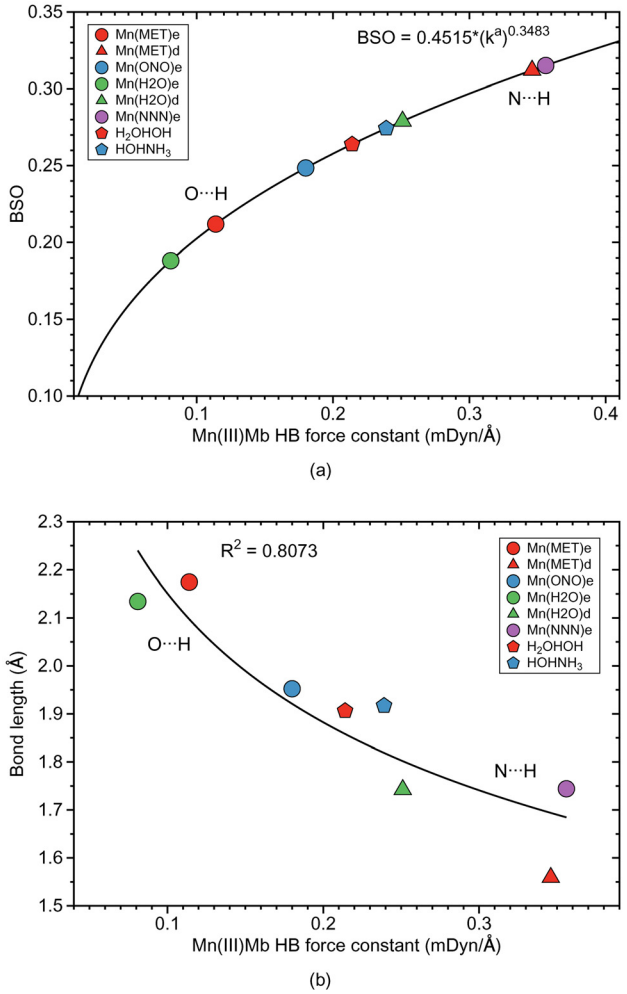

Fig. 9 HB properties of Mn(III)Mb–ligand complexes and corresponding properties of the water and water–ammonia molecular complexes. (a) Bond strength order BSO calculated from local mode force constants k^a *via* the generalized Badger rule. (b) Relation between local mode force constant k^a and bond length R. For molecular labels, see text.

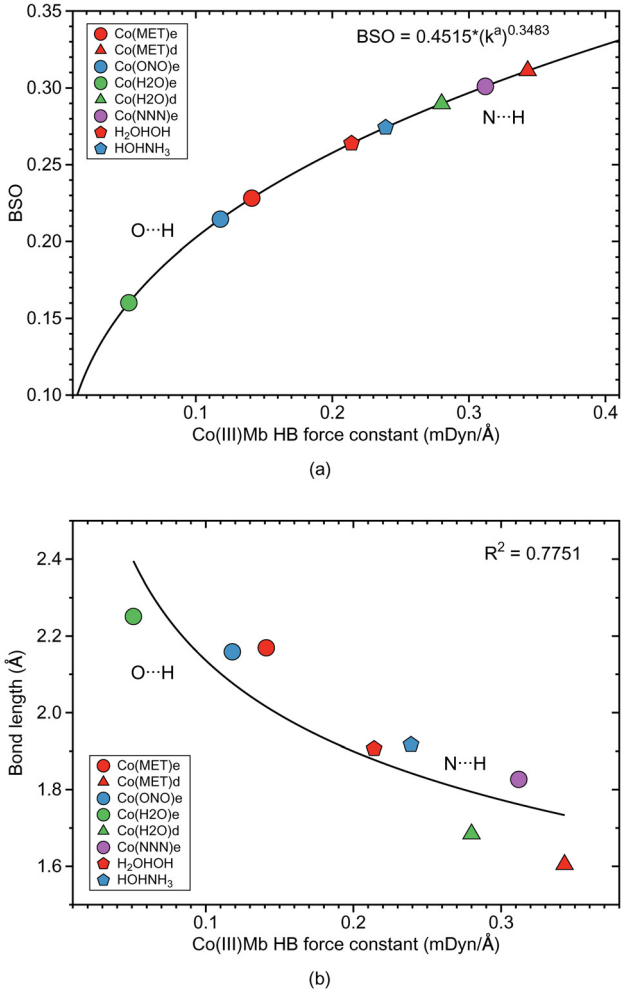

Fig. 10 HB properties of CO(III)Mb–ligand complexes and corresponding properties of the water and water–ammonia molecular complexes. (a) Relationship between local mode force constant k^a and BSO. (b) Relation between local mode force constant k^a and bond length R. For molecular labels, see text.

addition, Fig. S3 of ESI† presents the correlation between HB force constant k^a and energy density H_ρ, as well the correlation between k^a and the charge difference between the two atoms involved in the HB.

Generally, for the Co(III)Mb–ligand complexes we observe the same trends as for the Fe(III)Mb–ligand systems with some exceptions. According to Fig. 10a, the weakest HBs of the O···H type are found for the ε form of the Co(III)Mb protein (**Co(MET)e**, **Co(ONO)e**, and **Co(H$_2$O)e**). The HB of the N···H type for the same ε protein system (**Co(NNN)e**), is one of the strongest HB in this series. Moreover, both δ Co(III)Mb proteins (**Co(MET)d** and **Co(H$_2$O)d**) form relatively strong HBs of the N···H type. Similarly as in the Fe(III)Mb and Mn(III)Mb protein systems, the weaker Co–ligand chemical bonds in the **Co(MET)e** and **Co(H$_2$O)e** are paired with the weaker HBs of the O···H type, however for the azide anion **Co(NNN)e**, both a strong Co–ligand bond and a strong N···H type HB are observed.

3.5 ε *versus* δ HB visualized by CNM

Additional insights into the difference between ε *versus* δ ligand–histidine HB determining *e.g.*, the orientation of small molecular ligands in the heme pocket can be gained *via* our CNM analysis, which decomposes the normal vibrational modes of a molecule into local mode parameters, and as such can identify how the atoms of a specific structural element or functional group move during a specific vibration.[49,50] However, it has to be noted that whereas LMA properties can be calculated for a restricted number of local mode parameters of interest, such as the HB force constants k^a (HB) and the ML bond constants k^a (ML) as in this work, CMN requires the proper choice of a chemically meaningful complete and non-redundant set of N_{vib} local mode parameters, with $N_{vib} = (3N - 6)$ for a non-linear and $(3N - 5)$ for a linear molecule being composed of N atoms. This can become unfeasible for systems with a large number of atoms ($N > 100$), or QM/MM

systems, where N_{vib} is determined from the total number of QM and MM atoms, when performed manually or starting from a large redundant coordinate set and applying some trial and error procedures. Our group has developed two methods in order to help in this situation; (i) the generalized subsystem vibrational analysis (GSVA) developed in our group[108,109] which projects out from the full N_{vib} QM/MM set the important QM vibrations and (ii) LModeAGen[67] which offers a convenient way for the generation of local mode parameters based on chemical graph theory.[110]

In the following the CNM analysis for the **Fe(MET)e** and **Fe(MET)d** complexes is discussed as an example. Both complexes contain 3049 atoms (103 QM atoms, 2946 MM atoms) leading to a total of N_{vib} = 9141. After the GSVA procedure extracting the 297 QM normal modes of interest, LModeAGen was applied to generated a set of local mode parameters. In Fig. 11a and b the CNM is shown in the range of 900–3000 cm^{-1} focusing on the different role of the methanol OH bond. Fig. 11a shows the CNM for **Fe(MET)e** where one of the distal histidine N–H bonds serves as HB donor and the methanol oxygen as HB acceptor, whereas the methanol OH bond is a spectator bond. Fig. 11b shows the CNM for **Fe(MET)d** where the distal histidine nitrogen atom serves as HB acceptor and methanol OH bond as HB donor.

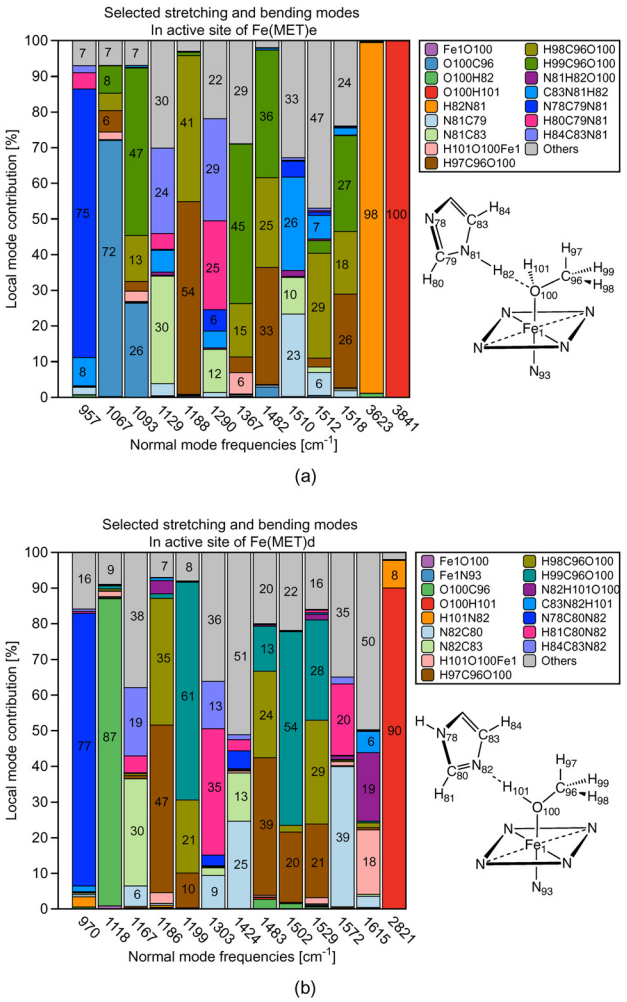

Fig. 11 Decomposition of normal vibrational modes into local stretching and bending contributions involved in O···H type and N···H type HB. (a) Fe(MET)e as representative for O···H type HB; (b) Fe(MET)d as representative for N···H type HB. For molecular labels, see text.

Fig. 11a clearly confirms the spectator character of the methanol OH bond in **Fe(MET)e**; the normal mode representing the methanol OH stretching vibration has 100% local OH stretching mode character, in line with the 3841 cm^{-1} OH stretching frequency, which is in the normal OH stretching range.[111] The NH bond of histidine serving as HB donor is with a frequency value of 3623 cm^{-1} some slightly redshifted,[111] but also has 98% local NH mode character. A different picture emerges for **Fe(MET)d** as revealed by the CNM shown in Fig. 11b. The methanol OH bond of **Fe(MET)d** serves as HB donor. As a consequence, the OH stretching frequency is considerably redshifted (2821 cm^{-1}). It has 90% local OH stretching character with an 8% admixture of N···H local mode stretching; elucidating the different scenarios of methanol OH bonding; qualifying CNM as a helpful tool for artificial Mb designers.

4 Conclusions and outlook

Based on comprehensive QM/MM calculations combined with LMA, we investigated the strength of ML bonding with methanol, water, nitrite, and azide as model ligands in the active site of Fe(III)Mb, Mn(III)Mb, and Co(III)Mb. This analysis was conducted for both the ε and δ forms of the distal histidine. In addition to ML bonding, we explored potential HB between the ligand and the distal histidine, a possibility that has not received much attention to date. To account for the effects of the protein environment, we also examined the corresponding gas-phase models of the protein active sites, using the same metals and ligands. HBs in the protein were compared with HBs in the water and water–ammonia molecular complexes.

As depicted in Fig. 12a the results of our study show that the two neutral ligands, methanol and water, form relatively weak ML bonds compared to their ionic counterparts, nitrite and azide, forming considerably stronger ML bonds. Moreover, ML bonds are weaker in the protein than in the gas phase models, which indicates that the protein environment influences ML bond formation/cleavage. The strength of the ML protein bonds also depends on the protonation form of the distal histidine, namely for the ε form of this residue the ML bond is generally weaker than that for the δ form (see Fig. 12a).

Overall, the average strength of the Co–ligand bonds (average k^a of 1.724 mDyn $Å^{-1}$) is greater than the average strength of Fe–ligand bonds (average k^a of 1.415 mDyn $Å^{-1}$) and that of Mn–ligand bonds (k^a of 0.882 mDyn $Å^{-1}$). These findings provide useful guidelines for fine-tuning of artificial Mbs with specific ML bond strengths. According to Fig. 12b summarizing the strength of the ML bonds for all three

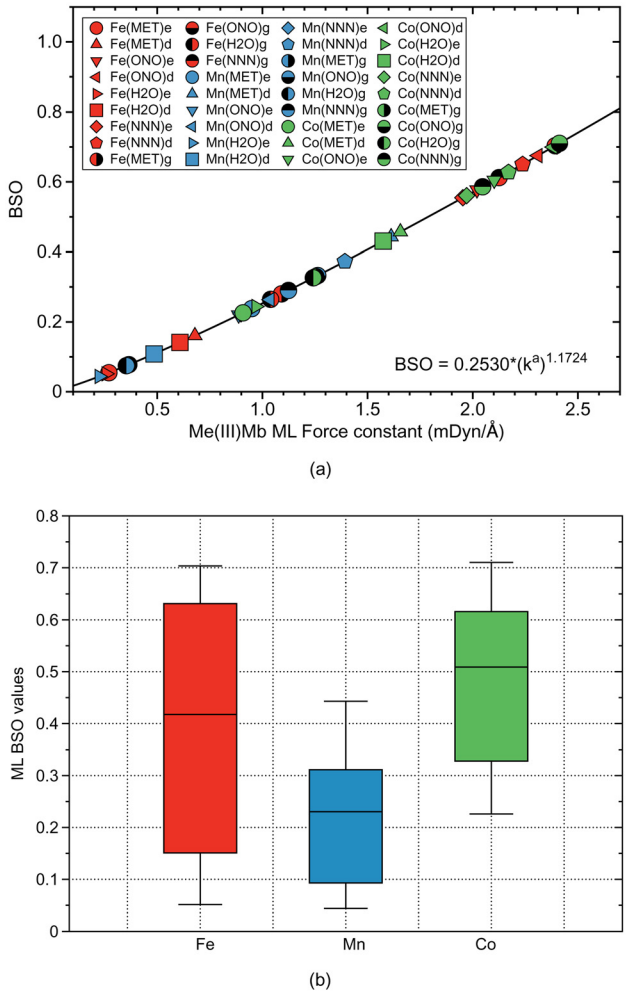

Fig. 12 (a) Bond strength order BSO calculated from local mode force constants k^a *via* the generalized Badger rule for all ML bonds of Mb complexes and gas phase models investigated in this study (Me = Fe, Mn, and Co). For molecular labels, see text. (b) Box and whisker plot of BSO values for all ML bonds investigated in this study.

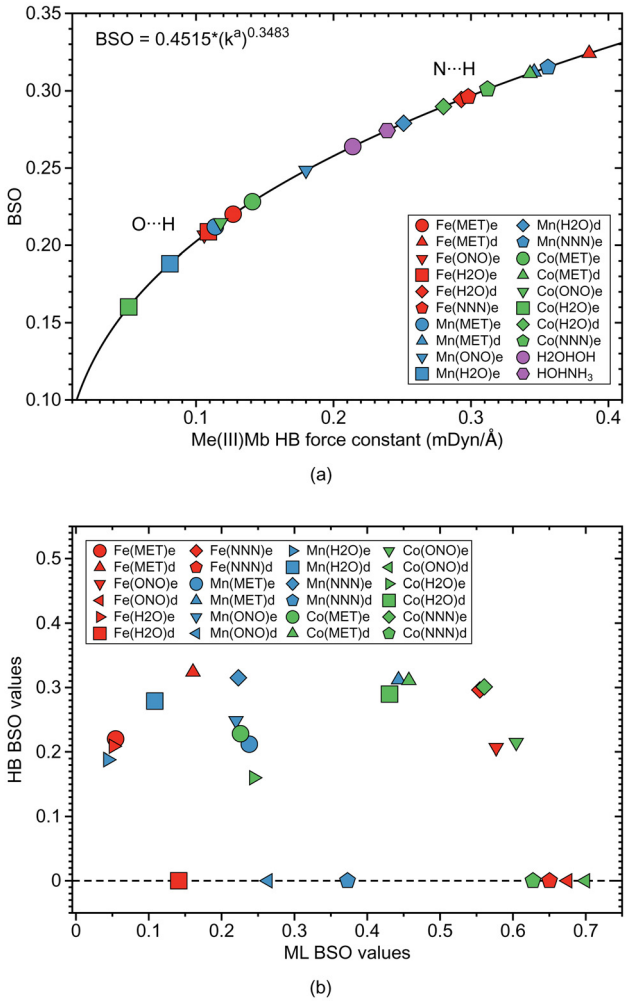

Fig. 13 (a) Bond strength order BSO calculated from local mode force constants k^a *via* the generalized Badger rule for all HB bonds of Mb complexes investigated in this study (Me = Fe, Mn, and Co). (b) Relation between ML and HB bond strengths for all Mb complexes investigated in this study. Zero HB BSO values indicate the lack of HB opportunity. For molecular labels, see text.

metals, the strength of the ML bonds with Fe covers a broader range than the other metals, which indicates that Fe should be selected as a candidate for a catalyst in chemical reactions that require ML bonds of different strengths.

For the ε histidine tautomer (see Fig. 13a) most ligands form O···H type HBs, where the distal histidine is the hydrogen atom donor, while for the δ tautomer N···H type HBs are formed with the distal histidine as HB acceptor. According to our calculations, the N···H type HBs are stronger and shorter in the proteins than in the reference water–ammonia pair, moving the ligands closer to the metal. However, as revealed by Fig. 13b we did not observe a direct correlation between ML and HB bond strengths.

The analysis of the HBs formed between the ligands and the distal histidine of Mb adds another layer of useful information, such as on the strength and covalency of HBs formed between ligand and histidine, with O···H type HBs overall weaker than their N···H type HB counterparts (see Fig. 13a) and how these HBs may influence the ligand orientation in the Mb pocket. We confirmed that stronger HBs are formed with the ionic ligands (nitrite and azide) compared to the neutral ones (methanol and water), which can be useful for the design of ionic reactants and intermediates of catalytic reactions taking place in the active site of Mb and/or its mutations.

A recent experimental investigation shows that replacing the native Mb porphine ring with a porphycene ring increases the protein's catalytic activity for the dehydration of various aldoximes.[112] These authors suggest that this enhancement is attributed to the involvement of the distal histidine in the reaction, and that a HB with the distal histidine determines the ligand's correct orientation, significantly reducing the reaction's activation energy. Furthermore, they propose that the hydrogen atom of histidine involved in the HB directly partici-

pates in the reaction, underscoring the crucial role of this HB in the overall reaction mechanism. We are currently exploring the mechanistic details with our Unified Reaction Valley Approach (URVA)[113,114] combined with LMA, which will provide a comprehensive, holistic picture. The results will be published in a forthcoming article.

In conclusion, our investigation provides in-depth insight into the strength of ML bonds formed between four prototype ligands (methanol, water, nitrite, and azide) and the metal centers in Fe, Mn, and Co myoglobins at the atomic level. As illustrated in the box-and-whisker plot in Fig. 12b, Fe exhibits a broader variation in ML bond strengths compared to Mn and Co. This suggests that Fe, the metal found in native myoglobin, is the most versatile candidate for designing artificial myoglobins for catalytic applications that require variable ML bond strengths. However, Mn, Co or other metals might still be preferable for specific synthetic reasons or in cases, such as PET-RAFT polymerization, where specific excitation of the metal is needed. Additionally, as shown in our study, analyzing potential HB interactions between ligands and the distal Mb histidine provides valuable insights into how small molecular ligands orient within the heme pocket. As revealed by our results this orientation is guided by the strength of the HBs formed with the distal histidine.

Overall, our findings identify the strength of both ML bonds and HBs, fully captured by LMA, as a key parameter determining the catalytic activity and function of Mbs. This is particularly relevant when considering neutral *versus* ionic ligands and other metals such as Mn or Co as alternatives to Fe. The insights gained through our investigation offer valuable guidance for strategically fine-tuning existing artificial Mbs and designing new, versatile variants. Specifically, bond strength combinations like those illustrated in Fig. 13b provide a practical roadmap for future exploration. We hope that our QM/MM-LMA protocol will become a valuable addition to the research community's toolkit.

Author contributions

Marek Freindorf (**https://orcid.org/0000-0001-5285-5455**): writing – review and editing, conceptualization, investigation, data curation, methodology; Elfi Kraka (**https://orcid.org/0000-0002-9658-5626**): writing – review and editing, conceptualization, funding acquisition, supervision.

Data availability

The data supporting this article have been included as part of the ESI.†

Conflicts of interest

There are no conflicts to declare.

Acknowledgements

We thank the SMU O'Donnell Data Science and Research Computing Institute for providing generous computational resources. This work was financially supported by the National Science Foundation, Grant CHE 2102461. We also thank Bangaru Bhaskararao and Juliana Antonio for fruitful discussions.

References

1 B. M. Hoffman, *The Porphyrins*, Academic Press, New York, 1979, vol. 7, pp. 403–444.
2 J. S. Olson, *Antioxid. Redox Signaling*, 2019, **32**, 228–246.
3 G. A. Ordway and D. J. Garry, *J. Exp. Biol.*, 2004, **207**, 3441–3446.
4 I. E. Elkholi, M. E. Elsherbiny and M. Emara, *Biochim. Biophys. Acta*, 2022, **1877**, 188706.
5 E. Zonetff, Y. Wang, C. Jackson, O. Smith, S. Duchi, C. Onofrillo, B. Farrugia, S. Moulton, R. Williams, C. Parish, D. R. Nisbet and L. M. Caballero-Aguilar, *Nat. Commun.*, 2024, **15**, 4361.
6 F. Darain, P. Yager, K. L. Gan and S. C. Tjin, *Biosens. Bioelectron.*, 2009, **24**, 1744–1750.
7 K. K. Adepu, A. Anishkin, S. H. Adams and S. V. Chintapalli, *Physiol. Rev.*, 2024, **104**, 1611–1642.
8 Y. Kagawa, K. Oohora and T. Hayashi, *J. Inorg. Biochem.*, 2024, **252**, 112459.
9 K. Oohora, A. Onoda and T. Hayashi, *Acc. Chem. Res.*, 2019, **52**, 945–954.
10 M. Tinzl, J. V. Diedrich, P. R. Mittl, M. Clémancey, M. Reiher, J. Proppe, J.-M. Latour and D. Hilvert, *J. Am. Chem. Soc.*, 2024, **146**, 1957–1966.
11 K. Yu and T. R. Ward, *J. Inorg. Biochem.*, 2024, **258**, 112621.1–112621.18.
12 W.-N. Xu, Y.-D. Gao, P. Su, L. Huang, Z.-L. He and L.-C. Yang, *ACS Catal.*, 2024, **14**, 14139–14160.
13 Y.-W. Lin, *J. Inorg. Biochem.*, 2024, **257**, 112595.1–112595.14.
14 M. Bordeaux, V. Tyagi and R. Fasan, *Angew. Chem.*, 2015, **127**, 1764–1768.
15 H. M. Key, P. Dydio, D. S. Clark and J. F. Hartwig, *Nature*, 2016, **534**, 534–537.
16 P. Dydio, H. M. Key, A. Nazarenko, J. Y.-E. Rha, V. Seyedkazemi, D. S. Clark and J. F. Hartwig, *Science*, 2016, **354**, 102–106.
17 G. Sreenilayam, E. J. Moore, V. Steck and R. Fasan, *Adv. Synth. Catal.*, 2017, **359**, 2076–2089.
18 Z. N. Zahran, L. Chooback, D. M. Copeland, A. H. West and G. B. Richter-Addo, *J. Inorg. Biochem.*, 2008, **102**, 216–233.
19 K. L. Stone and S. M. Ahmed, *Inorganics*, 2016, **4**, e12.1–e12.16.
20 R. Lin, C. E. Immoos and P. J. Farmer, *J. Biol. Inorg. Chem.*, 2000, **5**, 738–747.

21 K. Oohora, Y. Kihira, E. Mizohata, T. Inoue and T. Hayashi, *J. Am. Chem. Soc.*, 2013, **135**, 17282–17285.
22 K. Oohora, H. Meichin, Y. Kihira, H. Sugimoto, Y. Shiro and T. Hayashi, *J. Am. Chem. Soc.*, 2017, **139**, 18460–18463.
23 K. L. Stone, J. Hua and H. Choudhry, *Inorganics*, 2015, **3**, 219–229.
24 T. M. Makris, K. v. Koenig, I. Schlichting and S. G. Sligar, *J. Inorg. Biochem.*, 2006, **100**, 507–518.
25 H. Hirao, K.-B. Cho and S. Shaik, *J. Biol. Inorg. Chem.*, 2008, **13**, 521–530.
26 S.-C. Chien, O. Shoji, Y. Morimoto and Y. Watanabe, *New J. Chem.*, 2017, **41**, 302–307.
27 N. Kawakami, O. Shoji and Y. Watanabe, *ChemBioChem*, 2012, **13**, 2045–2047.
28 K. Omura, Y. Aiba, H. Onoda, J. K. Stanfield, S. Ariyasu, H. Sugimoto, Y. Shiro, O. Shoji and Y. Watanabe, *Chem. Commun.*, 2018, **54**, 7892–7895.
29 K. Omura, Y. Aiba, K. Suzuki, S. Ariyasu, H. Sugimoto and O. Shoji, *ACS Catal.*, 2022, **12**, 11108–11117.
30 S. I. Mann, A. Nayak, G. T. Gassner, M. J. Therien and W. F. DeGrado, *J. Am. Chem. Soc.*, 2021, **143**, 252–259.
31 I. Degtyarenko, R. M. Nieminen and C. Rovira, *Biophys. J.*, 2006, **91**, 2024–2034.
32 S. Neya, M. Suzuki, T. Hoshino and A. T. Kawaguchi, *Inorg. Chem.*, 2013, **52**, 7387–7393.
33 T. D. Rapson, S. Warneke, M. M. Musameh, H. Dacres, B. C. T. Macdonald and S. C. Trowell, *RSC Adv.*, 2015, **5**, 89003–89008.
34 Y. Morita, K. Oohora, E. Mizohata, A. Sawada, T. Kamachi, K. Yoshizawa, T. Inoue and T. Hayashi, *Inorg. Chem.*, 2016, **55**, 1287–1295.
35 A. T. Smith, T. Majtan, K. M. Freeman, Y. Su, J. P. Kraus and J. N. Burstyn, *Inorg. Chem.*, 2011, **50**, 4417–4427.
36 J. G. Kleingardner, B. Kandemir and K. L. Bren, *J. Am. Chem. Soc.*, 2014, **136**, 4–7.
37 D. J. Sommer, M. D. Vaughn, B. C. Clark, J. Tomlin, A. Roy and G. Ghirlanda, *Biochim. Biophys. Acta*, 2016, **1857**, 598–603.
38 K. Kitanishi, M. Shimonaka and M. Unno, *ACS Omega*, 2021, **6**, 34912–34919.
39 L. J. Perkins, B. R. Weaver, A. R. Buller and J. N. Burstyn, *Proc. Natl. Acad. Sci. U. S. A.*, 2021, **118**, e2017625118.
40 M. Meglioli, G. Di Rocco, A. Ranieri, C. A. Bortolotti, M. Sola, G. Battistuzzi and M. Borsari, *ChemElectroChem*, 2024, **11**, e202300821.
41 V. Firpo, J. M. Le, V. Pavone, A. Lombardi and K. L. Bren, *Chem. Sci.*, 2018, **9**, 8582–8589.
42 R. J. Labidi, B. Faivre, P. Carpentier, J. Perard, P. Gotico, Y. Li, M. Atta and M. Fontecave, *J. Am. Chem. Soc.*, 2024, **146**, 28296–28305.
43 I. C. Anderson, D. C. Gomez, M. Zhang, S. J. Koehler and C. A. Figg, *Angew. Chem., Int. Ed.*, 2024, e202414431.
44 C. E. Tzeliou, M. A. Mermigki and D. Tzeli, *Molecules*, 2022, **27**, 2660.
45 M. W. van der Kamp and A. J. Mulholland, *Biochemistry*, 2013, **52**, 2708–2728.
46 V. Guallar and F. H. Wallrapp, *Biophys. Chem.*, 2010, **149**, 1–11.
47 A. Warshel and M. Levitt, *J. Mol. Biol.*, 1976, **103**, 227–249.
48 A. Warshel and M. Karplus, *J. Am. Chem. Soc.*, 1972, **94**, 5612–5625.
49 E. Kraka, W. Zou and Y. Tao, *Wiley Interdiscip. Rev.: Comput. Mol. Sci.*, 2020, **10**, 1480.
50 E. Kraka, M. Quintano, H. W. La Force, J. J. Antonio and M. Freindorf, *J. Phys. Chem. A*, 2022, **126**, 8781–8798.
51 R. F. W. Bader, *Monatsh. Chem.*, 2005, **136**, 819–854.
52 R. F. W. Bader, *Atoms in Molecules: A Quantum Theory (International Series of Monographs on Chemistry)*, Clarendon Press, 1994.
53 R. F. W. Bader, *Chem. Rev.*, 1991, **91**, 893–928.
54 A. E. Reed, L. A. Curtiss and F. Weinhold, *Chem. Rev.*, 1988, **88**, 899–926.
55 F. Weinhold and C. R. Landis, *Valency and Bonding: A Natural Bond Orbital Donor-Acceptor Perspective*, Cambridge University Press, 2005.
56 J. D. Kelley and J. J. Leventhal, in *Problems in Classical and Quantum Mechanics: Normal Modes and Coordinates*, Springer, 2017, pp. 95–117.
57 E. Wilson, J. Decius and P. Cross, *Molecular Vibrations. The Theory of Infrared and Raman Vibrational Spectra*, McGraw-Hill, New York, 1955.
58 Z. Konkoli and D. Cremer, *Int. J. Quantum Chem.*, 1998, **67**, 1–9.
59 Z. Konkoli, J. A. Larsson and D. Cremer, *Int. J. Quantum Chem.*, 1998, **67**, 11–27.
60 E. B. Wilson, *J. Chem. Phys.*, 1941, **9**, 76–84.
61 E. Wilson, J. Decius and P. Cross, *Molecular Vibrations. The Theory of Infrared and Raman Vibrational Spectra*, McGraw-Hill, New York, 1955.
62 V. Barone, S. Alessandrini, M. Biczysko, J. R. Cheeseman, D. C. Clary, A. B. McCoy, R. J. DiRisio, F. Neese, M. Melosso and C. Puzzarini, *Nat. Rev. Methods Primers*, 2021, **1**, 38.
63 W. Zou and D. Cremer, *Theor. Chem. Acc.*, 2014, **133**, 1451–1466.
64 M. Freindorf and E. Kraka, *J. Mol. Model.*, 2020, **26**, 281-1–281-15.
65 M. Freindorf, A. A. A. Delgado and E. Kraka, *J. Comput. Chem.*, 2022, **43**, 1725–1746.
66 A. Madushanka, N. Verma, M. Freindorf and E. Kraka, *Int. J. Mol. Sci.*, 2022, **23**, 12310–1–12310–25.
67 R. T. Moura, Jr., M. Quintano, J. J. Antonio, M. Freindorf and E. Kraka, *J. Phys. Chem. A*, 2022, **126**, 9313–9331.
68 J. J. Antonio and E. Kraka, *Biochemistry*, 2023, **62**, 2325–2337.
69 M. Freindorf, J. Antonio and E. Kraka, *J. Phys. Chem. A*, 2023, **127**, 8316–8329.

70 M. Freindorf, J. Antonio and E. Kraka, *J. Comput. Chem.*, 2024, **45**, 574–588.
71 Y. Dangat, M. Freindorf and E. Kraka, *J. Am. Chem. Soc.*, 2024, **146**, 145–158.
72 Z. Konkoli and D. Cremer, *Int. J. Quantum Chem.*, 1998, **67**, 29–40.
73 Z. Konkoli, J. A. Larsson and D. Cremer, *Int. J. Quantum Chem.*, 1998, **67**, 41–55.
74 N. Verma, Y. Tao, W. Zou, X. Chen, X. Chen, M. Freindorf and E. Kraka, *Sensors*, 2020, **20**, 2358.
75 M. Quintano, A. A. A. Delgado, R. T. Moura Jr, M. Freindorf and E. Kraka, *Electron. Struct.*, 2022, **4**, 044005-1–044005-17.
76 M. Quintano, R. T. Moura Jr. and E. Kraka, *Chem. Phys. Lett.*, 2024, **849**, 141416.
77 W. Zou and D. Cremer, *Chem. – Eur. J.*, 2016, **22**, 4087–4099.
78 D. Cremer and E. Kraka, *Curr. Org. Chem.*, 2010, **14**, 1524–1560.
79 E. Kraka, J. A. Larsson and D. Cremer, *Computational Spectroscopy*, Wiley, New York, 2010, pp. 105–149.
80 I. Mayer, *Chem. Phys. Lett.*, 1983, **97**, 270–274.
81 I. Mayer, *Int. J. Quantum Chem.*, 1986, **29**, 477–483.
82 I. Mayer, *J. Comput. Chem.*, 2007, **28**, 204–221.
83 E. Kraka and M. Freindorf, *Reference Module in Chemistry, Molecular Sciences and Chemical Engineering - Comprehensive Computational Chemistry*, Elsevier, Heidelberg, 2022, pp. 1–27.
84 D. Cremer and E. Kraka, *Angew. Chem., Int. Ed. Engl.*, 1984, **23**, 627–628.
85 D. Cremer and E. Kraka, *Croat. Chem. Acta*, 1984, **57**, 1259–1281.
86 F. Weinhold, C. R. Landis and E. D. Glendening, *Int. Rev. Phys. Chem.*, 2016, **35**, 399–440.
87 D. A. Case, I. Y. Ben-Shalom, S. R. Brozell, D. S. Cerutti, T. E. Cheatham, V. W. D. Cruzeiro, T. A. Darden, R. E. Duke, D. Ghoreishi, M. K. Gilson, H. Gohlke, A. W. Goetz, D. Greene, R. Harris, N. Homeyer, S. Izadi, A. Kovalenko, T. Kurtzman, T. S. Lee, S. LeGrand, P. Li, C. Lin, J. Liu, T. Luchko, R. Luo, D. J. Mermelstein, K. M. Merz, Y. Miao, G. Monard, C. Nguyen, H. Nguyen, I. Omelyan, A. Onufriev, F. Pan, R. Qi, D. R. Roe, A. Roitberg, C. Sagui, S. Schott-Verdugo, J. Shen, C. L. Simmerling, J. Smith, R. Salomon-Ferrer, J. Swails, R. C. Walker, J. Wang, H. Wei, R. M. Wolf, X. Wu, L. Xiao, D. M. York and P. A. Kollman, *AMBER*, University of California, San Francisco, 2018.
88 W. L. Jorgensen, J. Chandrasekhar, J. D. Madura, R. W. Impey and M. L. Klein, *J. Chem. Phys.*, 1983, **79**, 926–935.
89 M. Ernzerhof and J. P. Perdew, *J. Chem. Phys.*, 1998, **109**, 3313–3320.
90 J. P. Perdew, K. Burke and M. Ernzerhof, *Phys. Rev. Lett.*, 1996, **77**, 3865–3868.
91 C. Adamo and V. Barone, *J. Chem. Phys.*, 1999, **110**, 6158–6170.
92 S. Zhao, Z.-H. Li, W.-N. Wang, Z.-P. Liu, K.-N. Fan, Y. Xie and H. F. Schaefer, *J. Chem. Phys.*, 2006, **124**, 184102.
93 C. J. Cramer and D. G. Truhlar, *Phys. Chem. Chem. Phys.*, 2009, **11**, 10757–10816.
94 S. Li, J. M. Hennigan, D. A. Dixon and K. A. Peterson, *J. Phys. Chem. A*, 2009, **113**, 7861–7877.
95 R. Ditchfield, W. J. Hehre and J. A. Pople, *J. Chem. Phys.*, 1971, **54**, 724–728.
96 L. W. Chung, W. M. C. Sameera, R. Ramozzi, A. J. Page, M. Hatanaka, G. P. Petrova, T. V. Harris, X. Li, Z. Ke, F. Liu, H.-B. Li, L. Ding and K. Morokuma, *Chem. Rev.*, 2015, **115**, 5678–5796.
97 M. K. Safo, G. P. Gupta, F. A. Walker and W. R. Scheidt, *J. Am. Chem. Soc.*, 1991, **113**, 5497–5510.
98 G. McLendon and K. Sandberg, *J. Biol. Chem.*, 1978, **253**, 3913–3917.
99 S. Della Longa, S. Pin, R. Cortès, A. V. Soldatov and B. Alpert, *Biophys. J.*, 1998, **75**, 3154–3162.
100 T. Harami, *J. Phys. Chem.*, 1979, **71**, 1309–1318.
101 R. Silaghi-Dumitrescu, D. A. Svistunenko, D. Cioloboc, C. Bischin, F. Scurtu and C. E. Cooper, *Nitric Oxide*, 2014, **42**, 32–39.
102 M. Sundararajan and F. Neese, *Inorg. Chem.*, 2015, **54**, 7209–7217.
103 R. Langley, P. Hambright, K. Alston and P. Neta, *Inorg. Chem.*, 1986, **25**, 114–117.
104 M. J. Frisch, G. W. Trucks, H. B. Schlegel, G. E. Scuseria, M. A. Robb, J. R. Cheeseman, G. Scalmani, V. Barone, G. A. Petersson, H. Nakatsuji, X. Li, M. Caricato, A. V. Marenich, J. Bloino, B. G. Janesko, R. Gomperts, B. Mennucci, H. P. Hratchian, J. V. Ortiz, A. F. Izmaylov, J. L. Sonnenberg, D. Williams-Young, F. Ding, F. Lipparini, F. Egidi, J. Goings, B. Peng, A. Petrone, T. Henderson, D. Ranasinghe, V. G. Zakrzewski, J. Gao, N. Rega, G. Zheng, W. Liang, M. Hada, M. Ehara, K. Toyota, R. Fukuda, J. Hasegawa, M. Ishida, T. Nakajima, Y. Honda, O. Kitao, H. Nakai, T. Vreven, K. Throssell, J. A. Montgomery Jr, J. E. Peralta, F. Ogliaro, M. J. Bearpark, J. J. Heyd, E. N. Brothers, K. N. Kudin, V. N. Staroverov, T. A. Keith, R. Kobayashi, J. Normand, K. Raghavachari, A. P. Rendell, J. C. Burant, S. S. Iyengar, J. Tomasi, M. Cossi, J. M. Millam, M. Klene, C. Adamo, R. Cammi, J. W. Ochterski, R. L. Martin, K. Morokuma, O. Farkas, J. B. Foresman and D. J. Fox, *Gaussian 16*, Gaussian Inc., Wallingford CT, 2016.
105 W. Zou, R. Moura, Jr., M. Quintano, F. Bodo, Y. Tao, M. Freindorf, M. Z. Makoś, N. Verma, D. Cremer and E. Kraka, *LModeA2023*, Computational and Theoretical Chemistry Group (CATCO), Southern Methodist University, Dallas, TX, USA, 2023.
106 T. A. Keith, *AIMALL*, TK Gristmill Software, Overland Park KS, 2017.
107 R. M. Badger, *J. Chem. Phys.*, 1934, **2**, 128–131.
108 Y. Tao, C. Tian, N. Verma, W. Zou, C. Wang, D. Cremer and E. Kraka, *J. Chem. Theory Comput.*, 2018, **14**, 2558–2569.

109 Y. Tao, W. Zou, S. Nanayakkara, M. Freindorf and E. Kraka, *Theor. Chem. Acc.*, 2021, **140**, 31-1–31-5.
110 M. Randić, M. Novič and D. Plavšić, *Solved and Unsolved Problems of Structural Chemistry*, CRC Press, Boca Raton, 2016.
111 M. Freindorf, E. Kraka and D. Cremer, *Int. J. Quantum Chem.*, 2012, **112**, 3174–3187.
112 S. Kato, M. Abe, H. Gröger and T. Hayashi, *ACS Catal.*, 2024, **14**, 13081–13087.
113 E. Kraka, J. J. Antonio and M. Freindorf, *Chem. Commun.*, 2023, **59**, 7151–7290.
114 E. Kraka, W. Zou, Y. Tao and M. Freindorf, *Catalysts*, 2020, **10**, 691.